AIAA SciTech
5-9 January 2015, Kissimmee, Florida
56th AIAA/ASCE/AHS/ASC Structures, Structural Dynamics, and Materials Conference

AN OVERVIEW OF THE NASA HIGH SPEED ASE PROJECT: AEROELASTIC ANALYSES OF A LOW-BOOM SUPERSONIC CONFIGURATION

Walter A. Silva[1], Antonio De La Garza[2], Scott Zink[2], Elias G. Bounajem[2], J. Christopher Johnson[2], Michael Buonanno[3], Mark D. Sanetrik[4], Pawel Chwalowski[4], Seung Y. Yoo[5], and Jiyoung Hur[6]

[1]Aeroelasticity Branch
NASA Langley Research Center
Hampton, Virginia, USA
Walter.A.Silva@nasa.gov

[2]Lockheed-Martin Aeronautics Company
Ft. Worth, Texas, USA

[3]Lockheed-Martin Aeronautics Company
Palmdale, California, USA

[4]Aeroelasticity Branch
NASA Langley Research Center
Hampton, Virginia, USA

[5]Control and Dynamics Branch
NASA Dryden Flight Research Center
Edwards, California, USA

[6]TEAMS2
NASA Langley Research Center
Hampton, VA, USA

Downloaded by NASA LANGLEY RESEARCH CENTRE on January 12, 2015 | http://arc.aiaa.org | DOI: 10.2514/6.2015-0684

Keywords: supersonic aeroservoelasticity, computational aeroelasticity, ROM.

Abstract:

An overview of NASA's High Speed Aeroservoelasticity (ASE) project is provided with a focus on recent computational aeroelastic analyses of a low-boom supersonic configuration developed by Lockheed-Martin and referred to as the N+2 configuration. The overview includes details of the computational models developed to date including a linear finite element model (FEM), linear unsteady aerodynamic models, structured/unstructured CFD grids, and CFD-based aeroelastic analyses. In addition, a summary of the work involving the development of aeroelastic Reduced-Order Models (ROMs) and the application of the CFL3D-ASE code that enables the inclusion of a control system within the CFL3Dv6 CFD code is presented.

1 INTRODUCTION

The unique structural configuration of supersonic aircraft combined with nonlinear aerodynamics and rigid-body effects often results in highly complex nonlinear aeroelastic/flight dynamics phenomena. These aeroelastic phenomena can affect ride quality, gust loads,

This material is declared a work of the U.S. Government and is not subject to copyright protection in the United States.

flutter, flight dynamics and control, and engine performance. The aeroelastic/flight dynamics phenomena simultaneously influence the airframe and propulsion system controls, producing undesirable effects on performance and flying characteristics.

These aeroservoelastic (ASE) phenomena need to be thoroughly understood in order for supersonic flight to be safe, efficient, and comfortable. In addition, there is an opportunity, through active controls, to exploit these phenomena for improved performance and efficiency. Analysis and design capabilities for slender supersonic aircraft may then be enhanced by including this new knowledge.

A vast body of analytical, computational, wind-tunnel, and flight data exist on the ASE characteristics of subsonic transport and supersonic fighter aircraft [1]. Systems for control of undesirable aeroelastic phenomena, such as suppression of flutter, have been demonstrated in the past [2–5]. Systems that exploit vehicle flexibility for improved performance, such as vehicle roll control beyond aileron reversal and wing load alleviation have also been demonstrated [6, 7].

Considerably less data are available for supersonic cruise configurations. In the mid- to late-1990s, as part of the High Speed Research (HSR) program, research was performed in the areas of computational and experimental aeroelasticity [8]. As part of this research, aeroelastic wind-tunnel models were designed, built, and tested in the Transonic Dynamics Tunnel (TDT). A remnant from the HSR program is the Semi-Span Super-Sonic Transport (S4T) [9], a very sophisticated, aeroelastically-scaled semispan wind-tunnel model based on the Technology Concept Aircraft (TCA) configuration equipped with three active surfaces (ride control vane, aileron, horizontal tail) and flow-through nacelles with flexible mounts. The model was designed so that it would flutter within the TDT operating boundary, making it an ideal testbed for investigating ASE issues associated with supersonic cruise configurations.

Under the auspices of the Supersonics Program under NASA's Fundamental Aeronautics Program (FAP), the S4T was the subject of four experiments in the TDT: two open-loop (no feedback control) tests and two closed-loop (with feedback control) tests over the span of three years between 2007 and 2010. A special session on the various aspects of the S4T program was organized for the AIAA Structures, Structural Dynamics, and Materials (SDM) conference held in 2012. The work involving the S4T was completed in 2012.

The Supersonics Program was renamed the High Speed Program. The High Speed Program, still a component of NASA's Fundamental Aeronautics Program (FAP), continues the original charter of the Supersonics Program, addressing the technical barriers to safe, efficient, and economical supersonic flight. One of the projects within the High Speed Program is the Aeroservoelasticity (ASE) project, tasked with addressing the aeroelastic (AE), aeroservoelastic (ASE), and aeropropulsoservoelastic (APSE) challenges associated with low-boom supersonic configurations. In order to address more realistic challenges associated with a full-span configuration, including rigid-body modes, the High Speed ASE project is now focusing on a full-span low-boom configuration.

A top priority for the High Speed ASE project is to develop the tools required to perform accurate, high fidelity computational AE, ASE, and APSE analyses in support of the design of future low-boom high speed civil aircraft. As a means of accomplishing that priority, the High Speed Program is working with Lockheed-Martin to conduct such

Downloaded by NASA LANGLEY RESEARCH CENTRE on January 12, 2015 | http://arc.aiaa.org | DOI: 10.2514/6.2015-0684

analyses. Under the NASA N+2 (two generations from present state) contract, Lockheed-Martin has developed a low-boom supersonic configuration and a detailed finite element model (FEM). An artist rendering of a view of the Lockheed-Martin N+2 configuration is presented in Figure 1. The goal of the N+2 effort is to develop and validate technologies for future civil supersonic airliners. Primary activities under this effort included Low Boom Wind Tunnel Testing, Propulsion System Maturation, Optimization Method Development, Structural and Aeroelastic Analysis, and System Studies.

Figure 1: Artist's concept of the Lockheed-Martin N+2 configuration.

In addition to the analysis of the N+2 configuration, the High Speed - ASE project is also involved in the development of APSE models. The development of an APSE model consists of the interconnection of a traditional ASE model (airframe model) with a dynamic engine model. Traditionally, these two models are developed and used separately by distinct disciplines (such as ASE and propulsion performance). The ultimate goal of this development is to be able to determine if the airframes flexibility has an effect on the thrust dynamics of the propulsion system, coupling back to the airframe flexibility modes as a closed loop system, in order to study performance like vehicle stability and ride quality.

This paper will address recent results not covered in the initial work by Silva et al [10]. The paper begins with a description of the N+2 configuration followed by a description of the structural sizing and analysis leading to a finite element model (FEM). Parametric studies that consist of inclusion of metallic components are discussed. Recent and updated linear aeroelastic analyses are presented as well. Structured and unstructured grids of the N+2 configuration are presented along with Euler (inviscid) results at a cruise condition. Finally, a summary of the work being performed in the area of ROM development and application of the CFL3D-ASE code is also discussed. The CFL3D-ASE code enables the inclusion of a control system directly in the CFD aeroelastic analysis. Results for a simple configuration are presented to demonstrate the capability.

Downloaded by NASA LANGLEY RESEARCH CENTRE on January 12, 2015 | http://arc.aiaa.org | DOI: 10.2514/6.2015-0684

2 N+2 CONFIGURATION

In this section, general performance characteristics of the N+2 configuration are presented. Presented in Figure 2 are four different views: a planform view (Figure 2(a)), a side view (Figure 2(b)), an isometric view (Figure 2(c)), and a front view (Figure 2(d)). Of particular interest are the three engines, one mounted aft and on top while the other two are mounted below and close to the fuselage. From an aeroelastic point of view, this arrangement would not seem to pose any obvious aeroelastic issues. In fact, the two engines mounted below offer some relief from possible aeroelastic issues by being installed close to the fuselage instead of further out on the span of the wing. However, having these large masses at the tail of a flexible fuselage is likely to cause some aeroelastic issues.

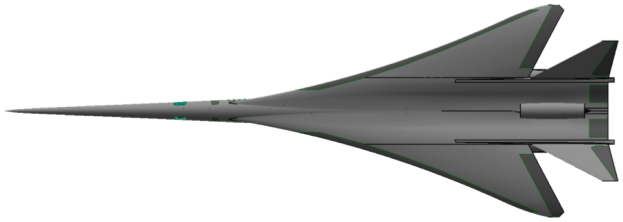

(a) Planform view.

(b) Side view.

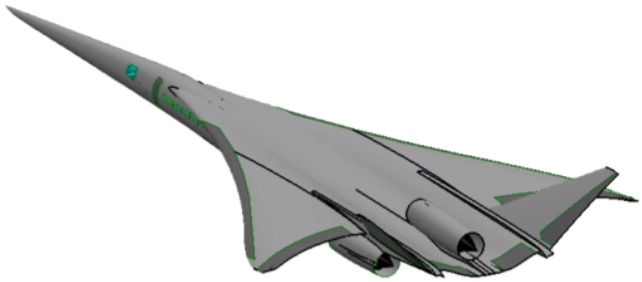

(c) Isometric view.

(d) Front view.

Figure 2: Different views of the N+2 configuration.

Downloaded by NASA LANGLEY RESEARCH CENTRE on January 12, 2015 | http://arc.aiaa.org | DOI: 10.2514/6.2015-0684

Presented in Table 1 are the general characteristics of the vehicle. At a length of 244 ft., the N+2 configuration is about 21% longer than the Concorde but at about the same wingspan. However, the N+2 configuration is lighter than the Concorde, with a cruising Mach number of 1.7 that is lower than that of the Concorde (cruise M=2.02), but with a greater range.

Table 1: N+2 Configuration

Length	244 ft.
Span	83 ft. 10 in.
Height	(Overall) 30 ft. 6 in. (Doorsill) 7 ft. 7 in.
Weight	(TOGW) 320,000 lbs. (Fuel) 168,000 lbs. (OEW) 136,000 lbs.
Cruise	M=1.7 L/D = 8.7
Payload	80 pax
Range	> 5000 nm
Boom Strength	(Full carpet) < 85 PLdB
Ground Op	(Wheelbase) 91 ft. 3 in. (Wheeltrack) 14 ft. (Turnover) 60 deg.

3 STRUCTURAL LAYOUT AND FEM

As a first step towards performing realistic aeroelastic analyses, Lockheed-Martin developed a detailed structural layout of the configuration. Presented in Figure 3 is a sample image of the substructure of the vehicle. The goal of the finite element modeling effort was to develop a structural model with a representative global stiffness and mass distribution to enable aeroelastic studies. To facilitate the use of high fidelity CFD based methods, a detailed structural layout was developed, meshed, and structurally optimized to a representative set of load cases consisting of landing, maneuver, and gust loads, subject to strain, buckling, and minimum gauge criteria. A combined image of all of the substructural components of the vehicle is presented in Figure 4.

Downloaded by NASA LANGLEY RESEARCH CENTRE on January 12, 2015 | http://arc.aiaa.org | DOI: 10.2514/6.2015-0684

Downloaded by NASA LANGLEY RESEARCH CENTRE on January 12, 2015 | http://arc.aiaa.org | DOI: 10.2514/6.2015-0684

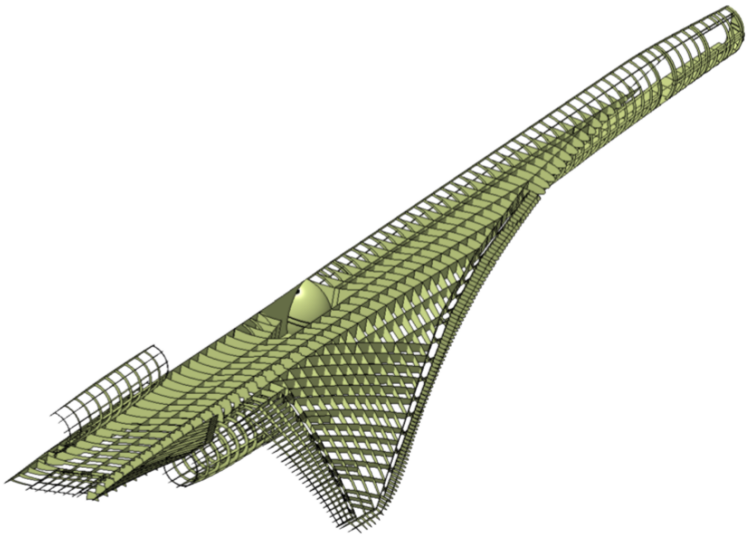

Figure 3: A view of the substructure of the N+2 configuration.

Based on this detailed structural layout, a detailed FEM was developed that captures realistic structural design constraints associated with this class of vehicles. A snapshot of the different sections of the N+2 FEM is presented as Figure 5.

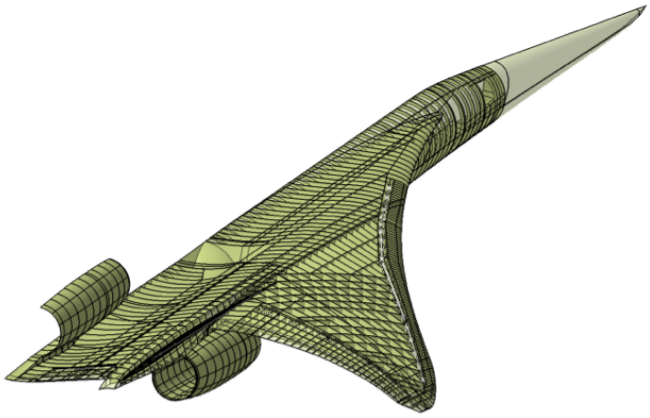

Figure 4: Structural layout of the N+2 configuration.

Downloaded by NASA LANGLEY RESEARCH CENTRE on January 12, 2015 | http://arc.aiaa.org | DOI: 10.2514/6.2015-0684

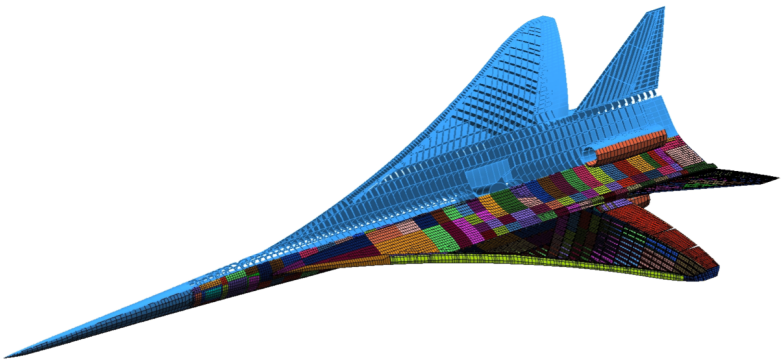

(a) Isometric view.

(b) Aft quarter.

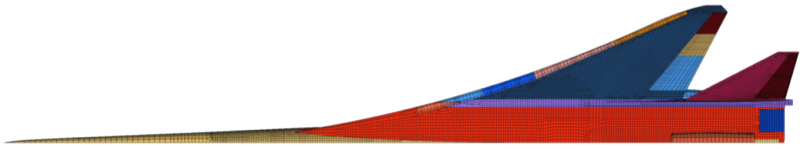

(c) Top view.

Figure 5: Different views of the N+2 FEM.

The finite element model was sized using MSC.Nastran [11] SOL200 assuming the implementation of composite structures. The majority of the FEM was discretized into constant property design zones, and the optimizer was allowed to adjust these properties using the design variables defined within these zones. The skins were assumed to utilize a sandwich approach consisting of Graphite/BMI Unidirectional Tape with a honeycomb core, resulting in three independent design variables per zone (0, ±45, 90 degree plies; core thickness remains constant in sizing). The design of the substructure also assumed

a sandwich approach with Graphite/BMI Fabric facesheets. The approach for the substructure assumed a quasi-isotropic laminate, resulting in one design variable per zone. Core thickness for the substructure also remained constant during sizing. A representative mass distribution was also developed and applied that accounted for systems, payload, and various fuel states. Buckling was included during the optimization by coupling an in-house analysis code along with MSC.Nastran SOL200.

The original all-composite FEM was updated to include metallic materials representative of material utilization on modern aircraft. Figure 6 summarizes the areas where metallics were used. The N+2 composition percentages were: composites 55%, aluminum 26%, titanium 16%, and steel 3%. The finite element model has roughly 170,000 degrees of freedom.

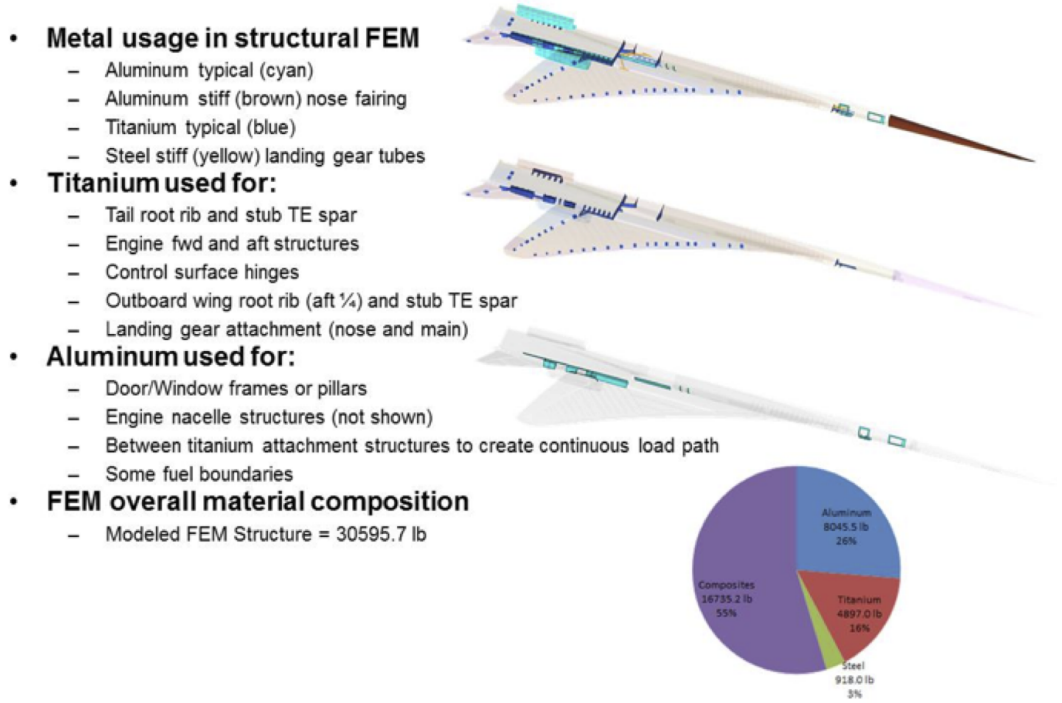

Figure 6: Metallic usage and overall composition of FEM.

In the course of sizing the N+2 vehicle, concerns arose over the tail and aft deck deflections under load. These concerns initiated an effort to modify the FEM to provide better load transfer from the tail to the centerline of the aft fuselage. Several options were considered and 3 modifications selected. These updates were accomplished by morphing the grid points of the original FEM to the new outer mold line geometry as follows:

1. Thicken the aft deck up to 50% of the local depth to increase stiffness of the aft deck substructure and the tail attachment.

2. Remove a sharp angle between the aft lower skin and the aft fuselage (referred to as a crease in the OML) to increase the minimum depth of the aft deck substructure.

3. Increase the tail T/C by 26% from 2.5% to 3.16% to reduce bending of the tail structure.

Downloaded by NASA LANGLEY RESEARCH CENTRE on January 12, 2015 | http://arc.aiaa.org | DOI: 10.2514/6.2015-0684

Structural sizing was done in MSC.NASTRAN SOL200, which utilizes gradient based optimization to determine optimal gauges that minimize weight while satisfying strength, buckling, and manufacturability criteria. Our in-house tool, AS3, serves as a front-end to the SOL200 optimization by translating design variable definition, stress/strain constraint definition, and buckling panel definition from a simple format to the NASTRAN bulkdata format. The buckling constraints are implemented through an external function call by SOL200 to our in-house panel buckling routine, TM1A, which assumes simply supported boundary conditions.

Design criteria for sizing the structure under the design loads consisted of stress/strain criteria, minimum gauge criteria, ply percentage criteria for composites, and buckling criteria. The strength criteria were knocked down from their room temperature allowable to account for an elevated temperature of 210 deg F, which corresponds to an adiabatic wall temperature at a cruise condition of Mach 2.0. The elements associated with skins were comprised of a Graphite composite tape system with 4 material directions, 0, 45, -45 and 90 deg directions, stiffened by honeycomb core. The thickness of each material direction was allowed to be a design variable, except that the +45 and -45 deg thickness were constrained to be equal in order to maintain a balanced laminate per composite design best practices. Thus there are 3 independent design variables for a composite skin design zone. The composite substructure (rib, spars, bulkheads, and longerons) were comprised of a Graphite composite fabric system, and these elements were enforced to be quasi-isotropic laminates (equal numbers of 0, 45, -45, and 90), since ribs and spars tend to be shear dominant. Thus, there is 1 independent design variable for a composite substructure property zone. For the metallic property zones, there is naturally only 1 design variable per zone, the thickness of the shell element, since metals are isotropic.

Thickness of the honeycomb core was not an independent design variable in the structural sizing process. As a result, a sizing trade study was initiated to look at variation in the core thickness and to identify the minimum weight core thickness on a global level. As shown in Figure 7, a sizing was conducted with various combinations of skin and substructure core thickness (ranging in increments of 0.75, 0.5 and 0.25). From the results of these studies, it was concluded that in general, 0.5 of core for the skins and 0.25 of core for the substructure was the minimum weight solution. Further optimization of the core thickness could be conducted for each panel, but was believed to have little impact on the overall aeroelastic characteristics of the vehicle.

Downloaded by NASA LANGLEY RESEARCH CENTRE on January 12, 2015 | http://arc.aiaa.org | DOI: 10.2514/6.2015-0684

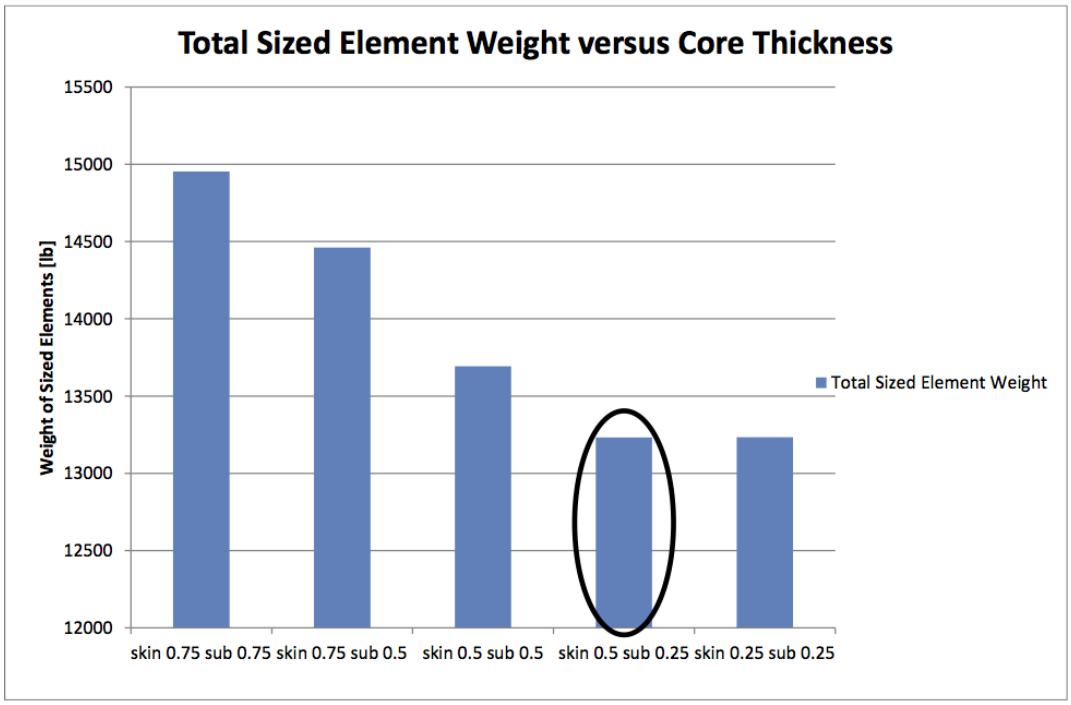

Figure 7: Core thickness trade study.

The FEM sized to strength, buckling and manufacturing criteria described above was designated FEM017-REV70. Upon analysis of this structural design to the design loads, we discovered that tail deformation for one of the pull-up maneuvers was excessive, nearly 47 inches for a tail span of roughly 250 inches. Consequently, a sizing analysis was performed where a constraint was added on tail deformation to be less than 25 inches (roughly 10% of the tail span). This FEM was designated FEM017-REV71. A comparison of the mass properties of each FEM is found in Figure 8. As seen in the table, the inclusion of the displacement constraint on the tail adds 1731 lb to the airframe weight, with most of it being added to the aft deck and the rest being added to the tail.

Downloaded by NASA LANGLEY RESEARCH CENTRE on January 12, 2015 | http://arc.aiaa.org | DOI: 10.2514/6.2015-0684

FULL SPAN	Mass Property Statement	FEM 017 Metal Rev70 SS Adjusted Mass	FEM 017 Metal Rev71 SS Adjusted Mass
Wing	*31504.0*	*24818.3*	*24755.2*
Aft Deck	*6934.0*	*4252.0*	*5371.6*
Tail	*4014.0*	*3703.3*	*4504.3*
Fuselage	*15086.0*	*11891.5*	*11764.9*
Subtotal	**57538.0**	**44665.2**	**46395.9**
Nacelle+Inlet (structure)	10946.0	12664.4	12664.4
NLG (structure + mass)	1377.0	1374.6	1374.6
MLG (structure + mass)	11096.0	11095.6	11095.6
Non-Fuel Sys Mass	76651.0	68007.0	68007.0
FEM Makeup Mass	0.0	19801.3	18070.6
Zero Fuel Weight	**157608.0**	**157608.1**	**157608.1**
Fuel Mass (updated)	175124.0	175124.0	175124.0
GTOW	**332732**	**332732**	**332732**
CG-X (Gear Up)	***2045.00***	***2021.75***	***2022.89***
CG-Y			
CG-Z	***257.10***	***258.39***	***258.51***

Figure 8: Weight summary of sized FEMs.

A modal solution was performed on the most recent FEM, the results of which with symmetric boundary conditions are in the following figures. Not shown are also three rigid body modes consistent with symmetric boundary conditions. The first four flexible symmetric modes are presented in Figure 9.

Downloaded by NASA LANGLEY RESEARCH CENTRE on January 12, 2015 | http://arc.aiaa.org | DOI: 10.2514/6.2015-0684

Downloaded by NASA LANGLEY RESEARCH CENTRE on January 12, 2015 | http://arc.aiaa.org | DOI: 10.2514/6.2015-0684

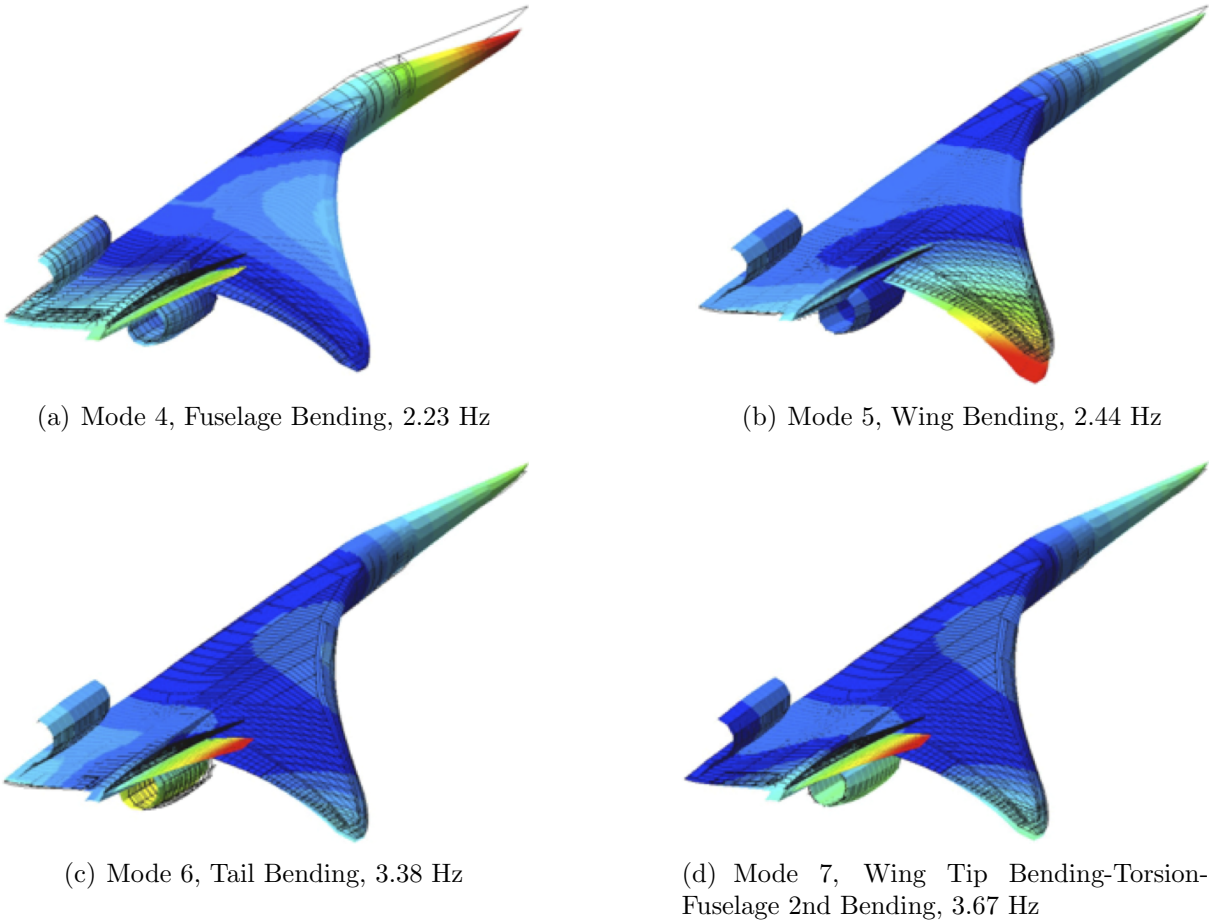

(a) Mode 4, Fuselage Bending, 2.23 Hz

(b) Mode 5, Wing Bending, 2.44 Hz

(c) Mode 6, Tail Bending, 3.38 Hz

(d) Mode 7, Wing Tip Bending-Torsion-Fuselage 2nd Bending, 3.67 Hz

Figure 9: First four symmetric flexible modes, Modes 4-7.

4 LINEAR AEROELASTIC ANALYSES

The N+2 configuration FEM is being used to perform linear and nonlinear AE analyses. This linear AE analyses include the generation of linear subsonic and supersonic frequency-domain unsteady aerodynamics. Presented in Figure 10 is a planform view of the doublet lattice aerodynamic box layout consisting of 1930 boxes.

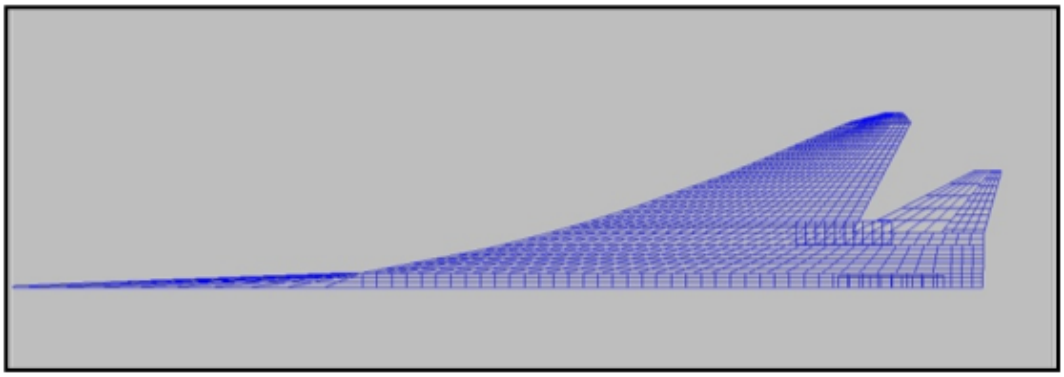

Figure 10: Planform view of the doublet lattice model.

External flight loads were computed via static aeroelastic analysis in MSC.NASTRAN (SOL144). The linear aerodynamic doublet-lattice method available in the solution was used and for initial loads calculations rigid aerodynamics were assumed, eventually transitioning to flexible aerodynamics as the structural design matured. Loads were also developed for a select number of cases using CFD (Euler) predictions.

Figure 11 presents the linear aerodynamic model used both for maneuver loads and flutter analyses. As shown in the figure, there are 9 control surfaces, 4 leading edge flaps (LEF), 2 ailerons, 1 trailing edge flap (TEF), 1 body flap and 1 rudder. For this semispan aerodynamic model there are 1930 individual aerodynamic boxes. Guidelines for developing the model included: avoiding abrupt element size changes between panels, maintaining streamwise continuity between panels (which required splitting the control surfaces into several pieces), and aiming for boxes with aspect ratios of 1 to 2 as much as possible without letting the number of elements become excessive. Mapping between the aerodynamic model and finite element model is provided via infinite plate splines.

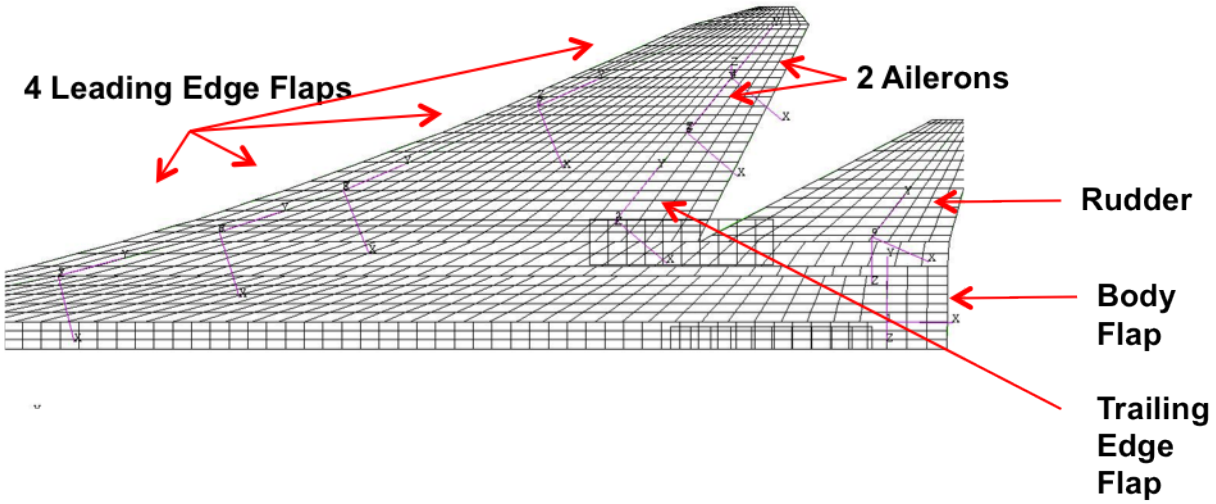

Figure 11: View of the control surface definitions for the doublet lattice model.

Figure 12 is a comparison of the lift curve as predicted by the linear aerodynamic model and compared to supersonic (Mach 1.7) wind tunnel test data. The linear aerodynamic model matches the measured lift curve quite well, especially when fuselage incidence and wing twist are removed from the model. Based on this data and the previous figure, the incidence and twist were included for subsonic maneuver load cases and removed for supersonic load cases.

Downloaded by NASA LANGLEY RESEARCH CENTRE on January 12, 2015 | http://arc.aiaa.org | DOI: 10.2514/6.2015-0684

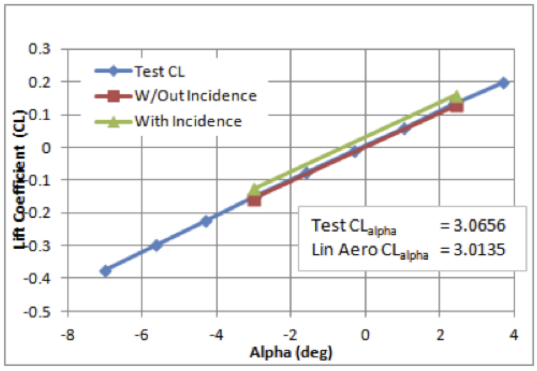

Figure 12: Comparison of linear aerodynamic lift coefficient with test data at Mach = 1.7.

Downloaded by NASA LANGLEY RESEARCH CENTRE on January 12, 2015 | http://arc.aiaa.org | DOI: 10.2514/6.2015-0684

Open-loop flutter analysis was performed on the final structural designs, FEM017-REV70 (sized without the constraint on tail displacement) and FEM017-REV71 (sized with the constraint on tail displacement). The MSC.NASTRAN SOL145 was used to compute flutter solutions, which uses the doublet lattice method for subsonic Mach numbers and the ZONA51 method for supersonic Mach numbers.

Flutter analysis was initially performed on the FEM017-REV71 structural design, the design that included a displacement constraint on tail deformation. However, for both symmetric and anti-symmetric boundary conditions and for three gross weights, there were no unstable flutter roots below 1600 psf and in most cases, especially for anti-symmetric boundary conditions, there were none below 3500 psf (minimum required flutter dynamic pressure is roughly 900 psf for most Mach numbers). This stood in stark contrast to previous flutter analyses on the all-composite FEM, where critical flutter dynamic pressures around 1000 psf were noticed. As a result, it was speculated that inclusion of the displacement constraint considerably stiffened the tail and aft deck thereby increasing the flutter speed dramatically, which was characterized largely by tail and aft deck bending. Consequently, flutter surveys were performed on the FEM017-REV70 design, which did not include the tail displacement constraints, and the results of these surveys are presented below, since the flutter speeds were much lower and closer to the flutter boundary.

Figure 13 shows the minimum flutter dynamic pressure as a function of Mach number and vehicle gross weight for symmetric boundary conditions. In addition, the minimum required flutter dynamic pressure (including the 15% margin on flutter speed) is represented by the solid red line. Flutter dynamic pressure below this line would indicate that the vehicle flutter requirement is not met, and so, based on this linear flutter analysis, we conclude that flutter speed is not critical. The dashed lines indicate that a flutter root was not found within the dynamic pressure range of the analysis (up to about roughly 4000 psf). However, in the transonic region, a more appropriate non-linear transonic flutter solver is needed. For the DTOW (Design Take-Off Weight) and DTOW2 (Design Take-Off Weight 2) flutter solutions, the flutter modes in the 3000-4000 psf range have a flutter frequency of about 10-12 Hz. The flutter modes that go unstable at lower dynamic pressure near 1500 2000 psf have flutter frequencies of about 5-6 Hz. The flutter frequency for the ZFW (Zero Fuel Weight) cases ranges from 6-7 Hz.

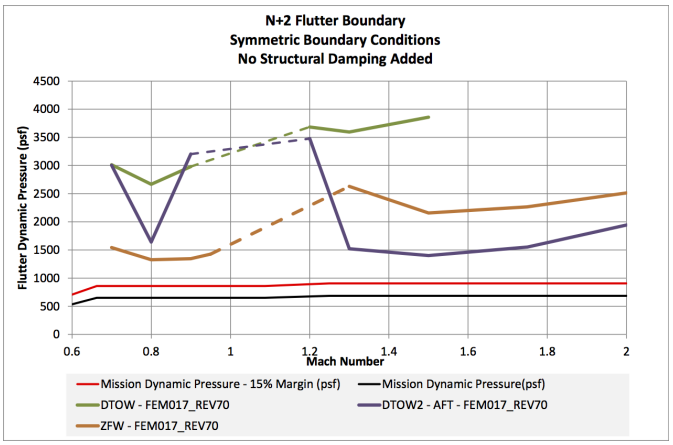

Figure 13: Flutter boundaries based on symmetric mode shapes and linear unsteady aerodynamics for different payload versions of the Rev70 FEM.

Figure 14 shows the minimum flutter dynamic pressure as a function of Mach number and vehicle gross weight for anti-symmetric boundary conditions. In general, the flutter speeds are higher than in the symmetric cases.

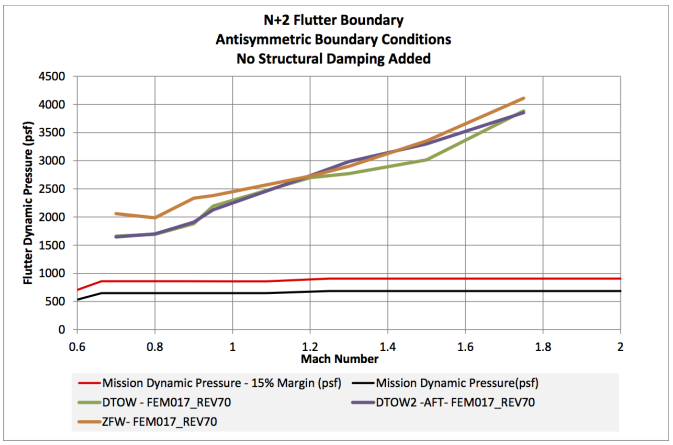

Figure 14: Flutter boundaries based on anti-symmetric mode shapes and linear unsteady aerodynamics for different versions of the FEM.

It can be seen that the most recent version of the FEM (FEM017-REV70) yields improved flutter boundaries across the Mach number range. It should be kept in mind that flutter dynamic pressures predicted by linear aerodynamics are less reliable in the transonic regime and are generally non-conservative. Exactly which Mach numbers define the transonic regime for this configuration is still to be determined. For these reasons, the use of CFD-based aeroelastic analyses becomes a critical part of this research.

Downloaded by NASA LANGLEY RESEARCH CENTRE on January 12, 2015 | http://arc.aiaa.org | DOI: 10.2514/6.2015-0684

5 CFD-BASED ANALYSES

A combination of CFD solvers were used, and continue to be used, to address the various goals of the N+2 effort. CFD++ from Metacomp Technologies was used for sonic boom analysis with a hybrid tet/hex grid tailored to efficiently propagate the pressure signatures to a sufficient distance for propagation to the ground. The Euler equations were solved for full scale sonic boom analysis due to the relatively small size of the boundary layer at high Reynolds number, but Navier Stokes analysis was found to be necessary for wind tunnel sonic boom prediction. For CFD-based loads, Splitflow [12] - a Lockheed-Martin in-house cartesian Euler/Navier Stokes Solver, was used to predict trim and aeroelastic effects on the load distribution. A Lockheed-Martin in-house modal-based linear structural analysis (LMMS) was used to perform the structural analysis and model control surface deflections. MDICE [13] (the MultiDisciplinary Computing Environment) was used to coordinate the simulation and transfer loads and displacements between Splitflow and LMMS.

CFD-based, trimmed flight loads were developed for select maneuver load cases. To accomplish this, a CFD loads model with sufficient detail to allow the actuation of control surfaces was developed. The baseline control surface scheme consisted of 4 leading edge flaps, 3 trailing edge flaps, a body flap, and a rudder. Due to spanwise camber on the wing, the wedge-shaped gaps between the trailing edge flaps were generated in order to allow deflection of the control surfaces without collision up to 30 degrees.

The trimmed CFD-based (Euler) maneuver loads were generated using LM Aeros computational aeroelasticity toolset, consisting of in-house aerodynamic and structural solvers linked together with the MultiDisciplinary Computing Environment (MDICE). The aerodynamic portion of the CFD-based aeroelastic analysis was performed using Splitflow. Figure 16 contains images of the surface mesh used by Splitflow. MDICE is used to coordinate the transfer of information between the aerodynamic and structural codes. MDICE uses an application programming interface (API) layer to link with analyses, transferring information between these processes in memory, thereby avoiding file-based transfer of data. MDICE also manages the execution of the simulation via a scripting language, thus enabling tailoring of the aeroelastic simulation to meet various goals and trim schemes.

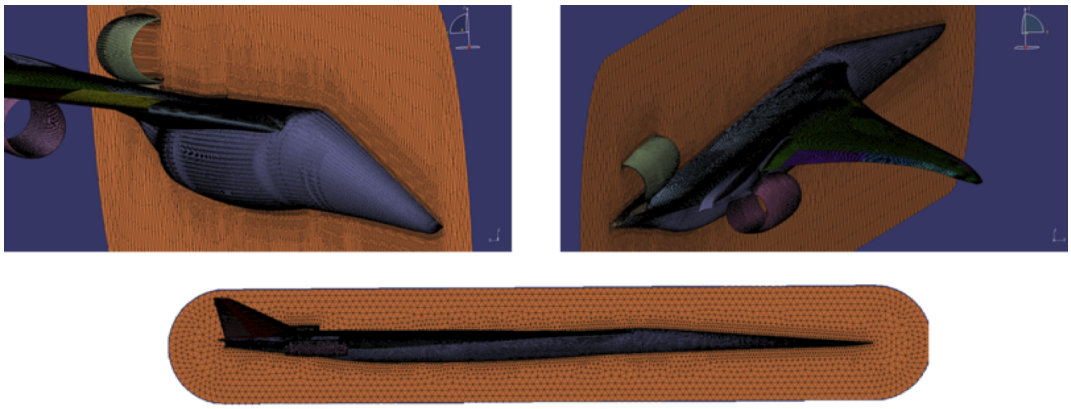

Figure 15: N+2 configuration 1044-3 surface mesh used by Splitflow for CFD-based aeroelastic analyses.

The structural portion of the aeroelastic analysis is handled by LMMS, which is a linear

Downloaded by NASA LANGLEY RESEARCH CENTRE on January 12, 2015 | http://arc.aiaa.org | DOI: 10.2514/6.2015-0684

structural analysis solver developed in-house. LMMS uses the normal modes computed by NASTRAN in combination with the nodes and element connectivity of the FEM to compute deflections due to loads transmitted from the aerodynamic analysis through MDICE. MDICE then maps the resulting deflections back to the aerodynamic grid in preparation for the next iteration of loads analysis. This process is repeated until convergence is achieved. LMMS also has utilities for computing deformation due to control surface deflections, which are superimposed on the elastic deflections before sending to MDICE. To develop trimmed flight loads, the overall vehicle force and moment coefficients are monitored during the aeroelastic simulation. An initial sensitivity analysis is done to develop coarse stability derivatives. Then a two degree of freedom trim problem (usually involving angle of attack and a trim surface deflection angle) is solved to compute a new trim state. This trim state is incrementally approached using a relaxation factor, which applies a fraction of the difference between the current and computed trim state as an update to the current trim state to avoid numerical instabilities.

Rigid CFD (Euler) trim solutions were generated for symmetric critical flight conditions. Good correlation between linear and CFD aerodynamics was obtained for subsonic and supersonic conditions at low angles of attack. Larger differences in the predicted trim state were noted at higher angles of attack. Vortex dominated flow features can be seen in the CFD-based results. Figure 17 shows the C_p distribution on the vehicle for a specific load case, clearly illustrating the vortex scrub pattern on the upper surface of the wing and vertical tail. Figure 18 shows iso-surfaces of vorticity magnitude colored by helicity, which gives more insight to the structure of the vortices for this condition. These effects can be seen in the applied loads once the pressures have been mapped to forces on the structural model.

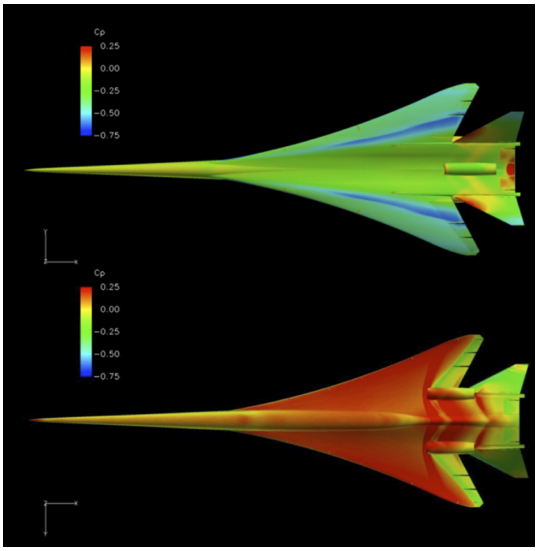

Figure 16: CFD-based C_p distribution illustrating vortex dominated effects on the upper surface at M=1.41, Alt=49.78kft, AOA=12.45 deg., with body flap and trailing edge surfaces set to -5.56 deg.

Downloaded by NASA LANGLEY RESEARCH CENTRE on January 12, 2015 | http://arc.aiaa.org | DOI: 10.2514/6.2015-0684

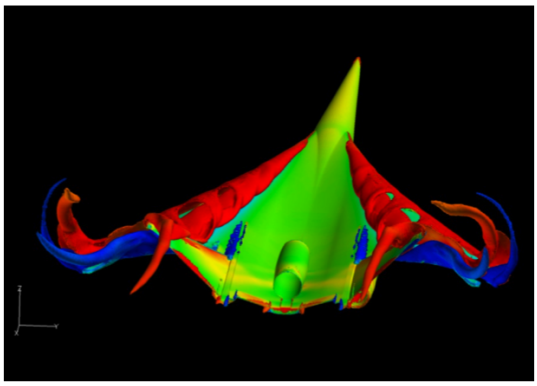

Figure 17: Iso-surfaces of vorticity magnitude illustrating vortical structures at M=1.41, 2.5 g load case.

Downloaded by NASA LANGLEY RESEARCH CENTRE on January 12, 2015 | http://arc.aiaa.org | DOI: 10.2514/6.2015-0684

For the CFD-based aeroelastic analyses, the Langley-developed CFD codes CFL3Dv6 (structured) and FUN3Dv12 (unstructured) are being applied. Structured and unstructured grids of the N+2 configuration have been generated.

5.1 Structured Grids

CFD-based aeroelastic analyses of the N+2 configuration have been generated using both a structured and an unstructured CFD code. The structured code to be used in this analysis is the CFL3Dv6 code.

The CFL3Dv6 code [14–16] solves the three-dimensional, thin-layer, Reynolds averaged Navier-Stokes equations with an upwind finite volume formulation. The code uses third-order upwind-biased spatial differencing for the inviscid terms with flux limiting in the presence of shocks. Either flux-difference splitting or flux-vector splitting is available. The flux-difference splitting method of Roe [17] is employed in the present computations to obtain fluxes at cell faces. There are two types of time discretization available in the code. The first-order backward time differencing is used for steady calculations while the second-order backward time differencing with subiterations is used for static and dynamic aeroelastic calculations. Furthermore, grid sequencing for steady state and multigrid and local pseudo-time stepping for time marching solutions are employed.

Presented in Figure 19 is a representative view of the structured surface grid currently under development for use with the CFL3Dv6 code. The structured surface grid has about 190,000 grid points. Multiple structured grids have been generated, both inviscid and viscous: one without engine nacelles and one with engine nacelles. Although the engines are always included via the mode shapes, the aerodynamic representation of the engine nacelles (in a grid) will not be included in one of the structured grids generated. The reason for generating a grid without the engine nacelles is based on prior experience. In the past, the creation of a structured grid for this class of vehicles with the inclusion of engine nacelles posed difficulties when splining the mode shapes onto the surface grid in the region of the engine nacelles. Whether or not the inclusion of engines in a structured grid will be a difficulty for this configuration is to be evaluated during this research.

Downloaded by NASA LANGLEY RESEARCH CENTRE on January 12, 2015 | http://arc.aiaa.org | DOI: 10.2514/6.2015-0684

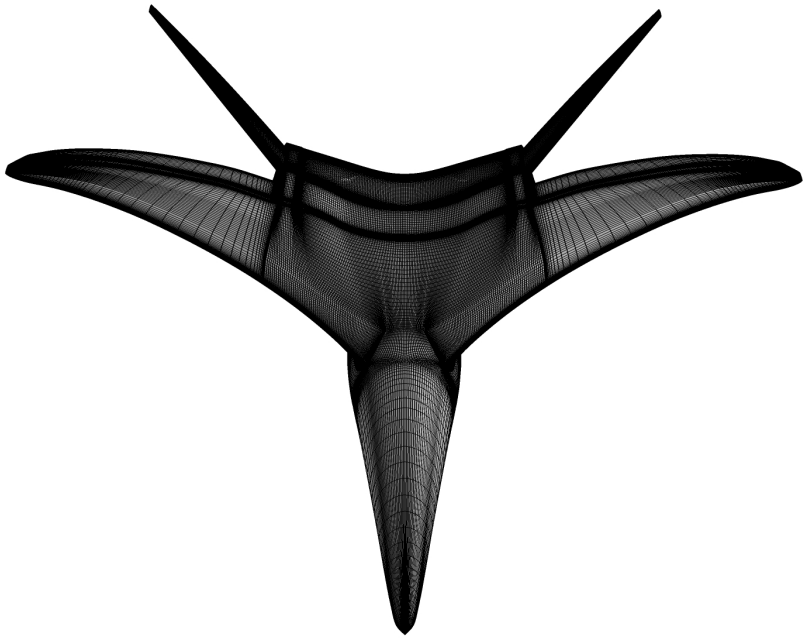

Figure 18: Forward and top view of the structured grid.

A sample steady Euler (inviscid) result for a rigid configuration computed using the CFL3Dv6 code at the start of the cruise condition is presented as Figure 20.

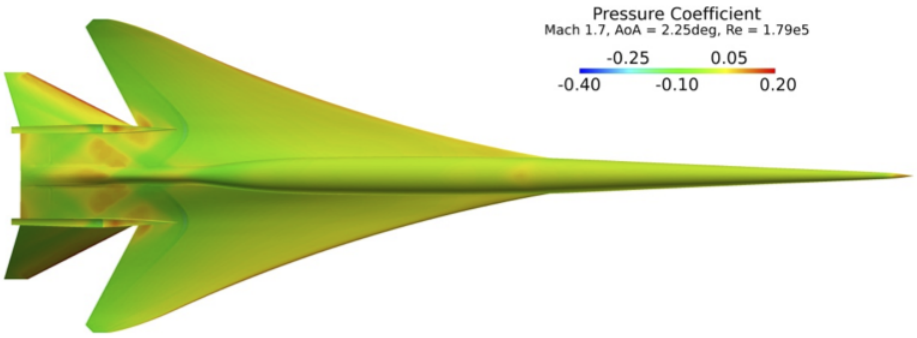

Figure 19: CFL3Dv6 Euler steady rigid computation at start of cruise condition.

5.2 Unstructured Grids

Unstructured grids of the N+2 configuration are also being generated for use with the FUN3Dv12 code [18]. The unstructured mesh solver used for this study is FUN3Dv12. Within the code, the unsteady Navier-Stokes equations are discretized over the median dual volume surrounding each mesh point, balancing the time rate of change of the aver-

aged conserved variables in each dual volume with the flux of mass, momentum and energy through the instantaneous surface of the control volume. Additional details regarding the aeroelastic capability within the FUN3Dv12 code can be found in the references [19].

Presented in Figure 21 is a forward view of the inviscid unstructured surface grid recently generated. The half-plane unstructured surface grid has 298,085 points and 555,710 cells.

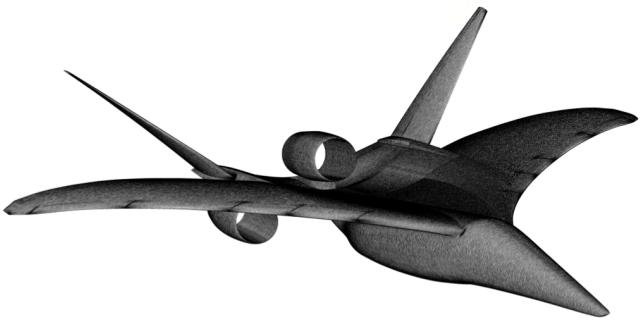

Figure 20: Forward view of the inviscid unstructured grid.

Grids that were generated initially were used for preliminary static aeroelastic analyses. However, these grids had to be modified and adapted in order to perform accurate sonic boom analyses. Therefore, the coarse grid used for the static aeroelastic analysis is not the same coarse grid that was used for the sonic boom analysis.

Presented in Figure 22 is a steady inviscid (Euler) FUN3Dv12 solution at cruise condition using a coarse grid. Presented in Figure 23 is a steady inviscid (Euler) FUN3Dv12 solution at cruise condition using a fine grid. Preliminary comparison of performance parameters between the two grids indicates very minor differences thereby permitting the use of the coarse grid for most analyses. Figure 24 presents a static aeroelastic computation for the FUN3Dv12 Euler (inviscid) coarse grid at cruise condition using the first 25 flexible modes. Results indicate a static aeroelastic deformation of about six inches at the wing tip and tail.

Downloaded by NASA LANGLEY RESEARCH CENTRE on January 12, 2015 | http://arc.aiaa.org | DOI: 10.2514/6.2015-0684

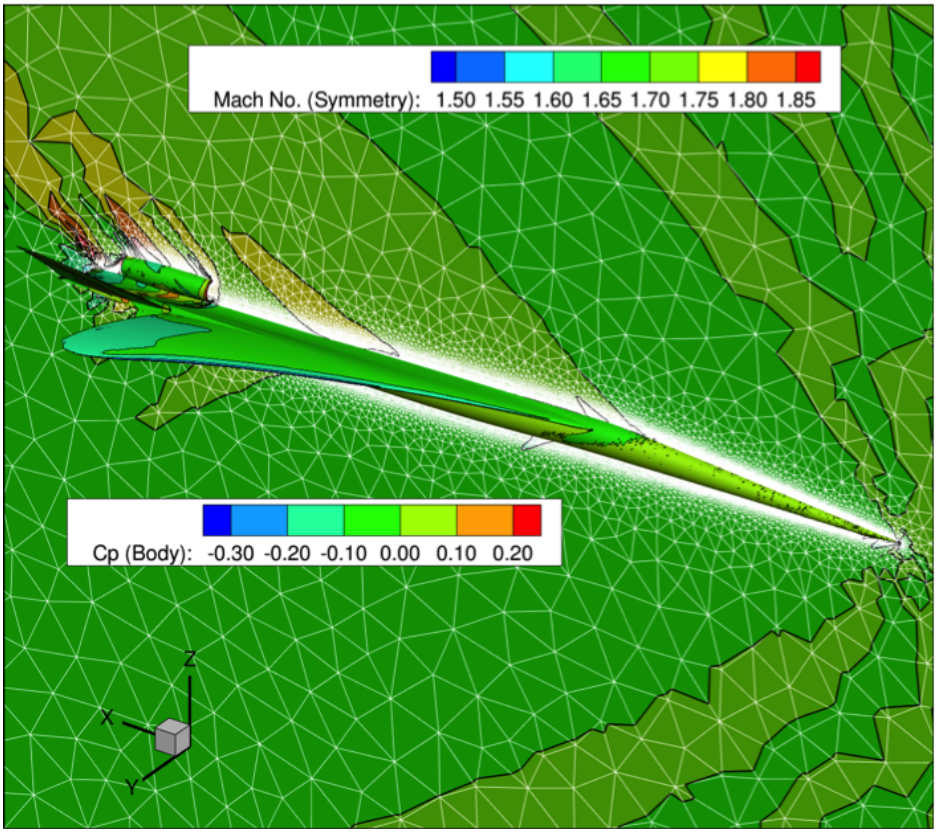

Figure 21: Coarse grid (5.4 million) FUN3Dv12 steady (undeformed) Euler (inviscid) result at cruise condition.

Downloaded by NASA LANGLEY RESEARCH CENTRE on January 12, 2015 | http://arc.aiaa.org | DOI: 10.2514/6.2015-0684

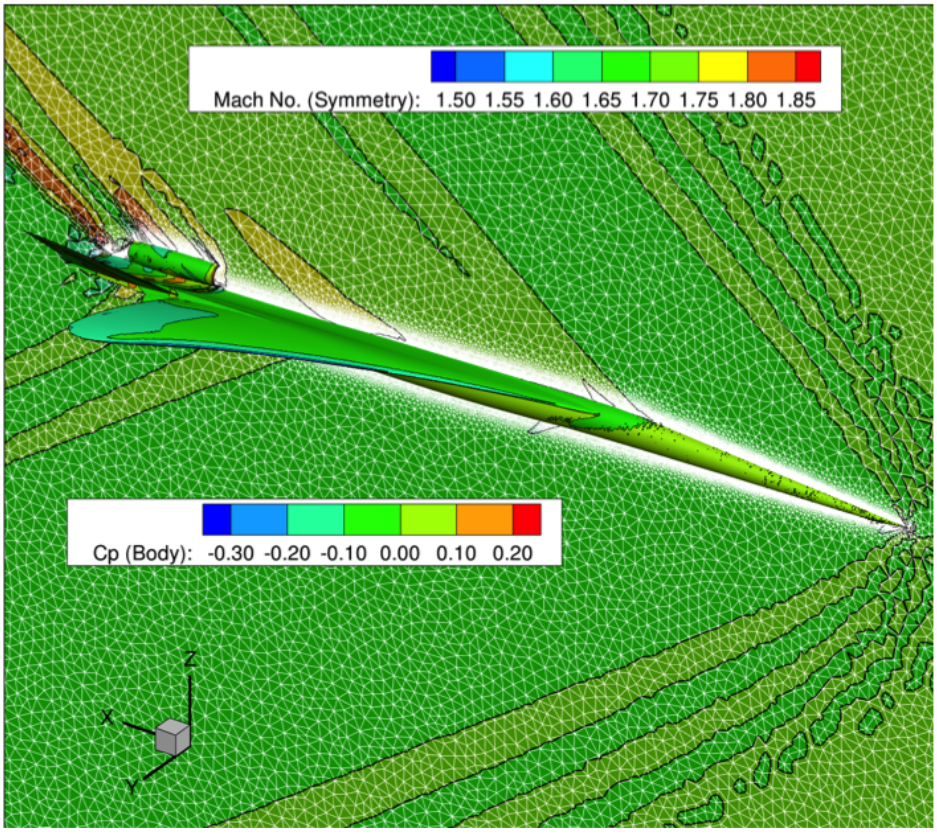

Figure 22: Fine grid (57.5 million) FUN3Dv12 steady (undeformed) Euler (inviscid) result at cruise condition.

Downloaded by NASA LANGLEY RESEARCH CENTRE on January 12, 2015 | http://arc.aiaa.org | DOI: 10.2514/6.2015-0684

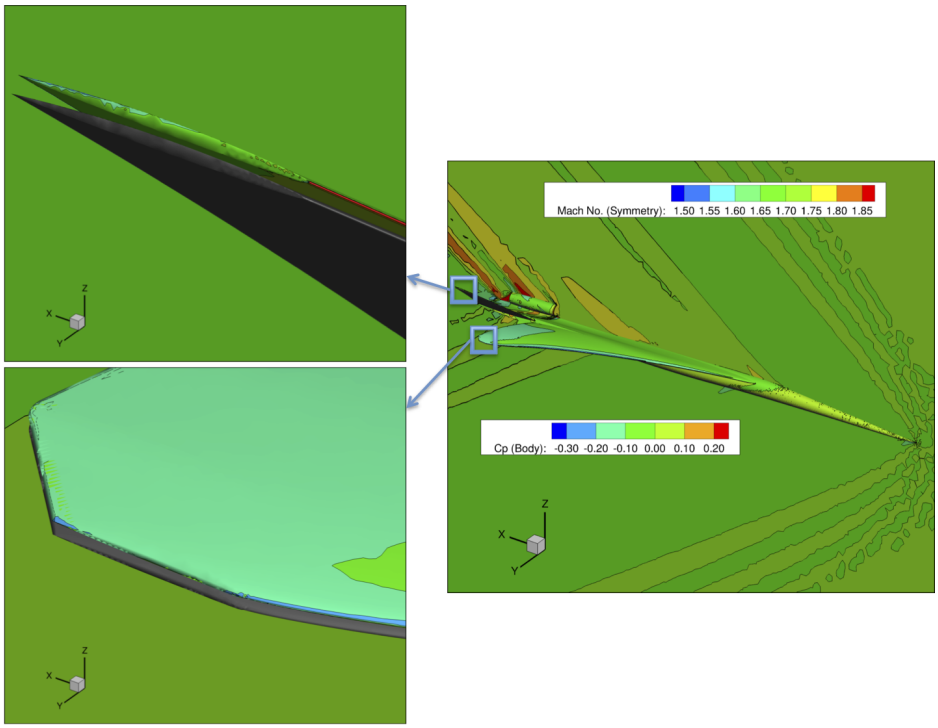

Figure 23: Coarse grid FUN3Dv12 static aeroelastic Euler (inviscid) deformation at the wing tip at cruise condition. Green surface is deformed shape.

In order to compute the effect of this static aeroelastic deformation on sonic boom, a near-field region is defined that is 8.25 half-spans away from the configuration at the cruise condition, presented in Figure 25.

Downloaded by NASA LANGLEY RESEARCH CENTRE on January 12, 2015 | http://arc.aiaa.org | DOI: 10.2514/6.2015-0684

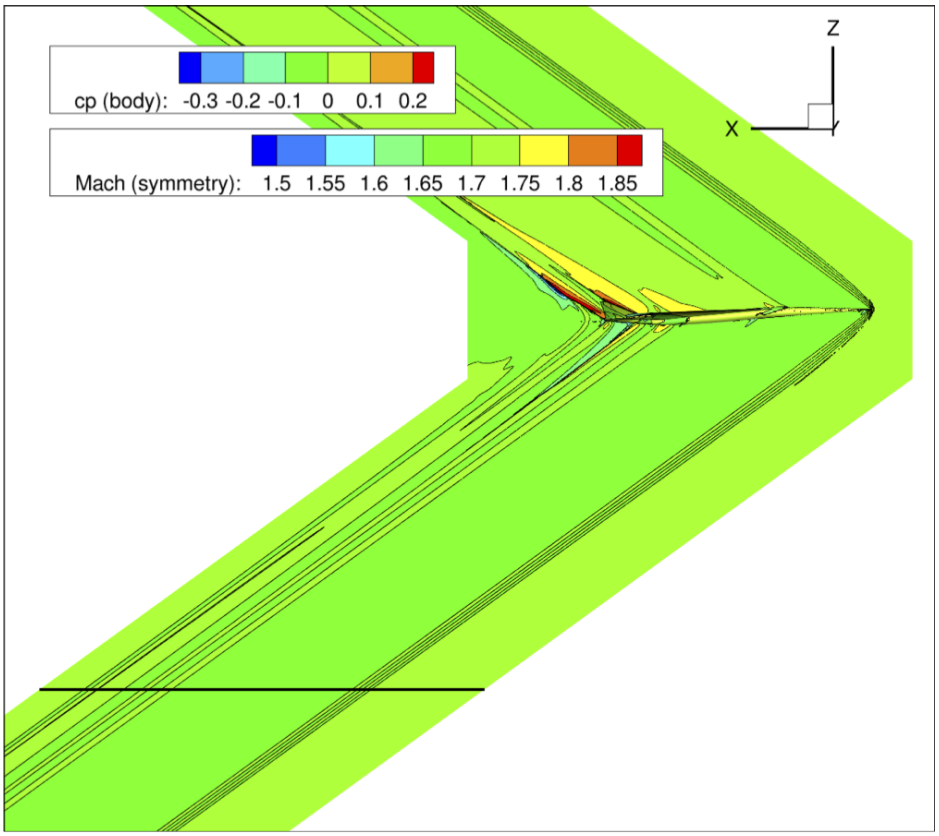

Figure 24: Coarse grid FUN3Dv12 steady (undeformed) Euler (inviscid) near field definition at 8.25 half-spans away at cruise condition.

A comparison of near-field pressure results at the prescribed near-field location for different grid densities (coarse, medium, and fine) is presented as Figure 26. There appear to be some slight differences for the coarse grid solution while the medium and fine grid solutions appear to be more closely correlated. Although the coarse grid is being used for these preliminary sonic boom assessments, solutions using the medium and fine density grids are currently underway.

Downloaded by NASA LANGLEY RESEARCH CENTRE on January 12, 2015 | http://arc.aiaa.org | DOI: 10.2514/6.2015-0684

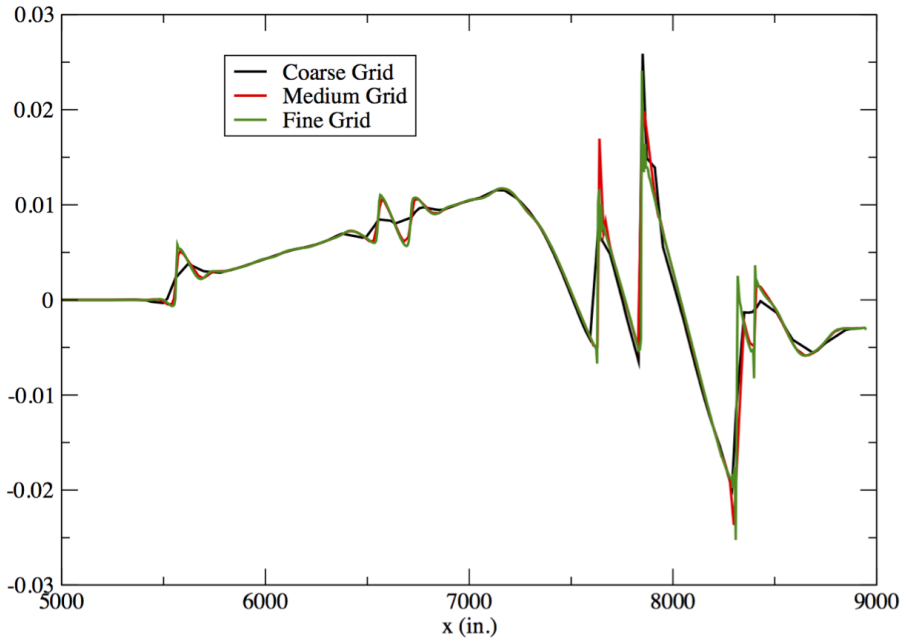

Figure 25: Near-field pressure distribution for the undeformed case for different grid densities.

Presented in Figure 27 is a comparison of the near-field pressure distributions for the undeformed and deformed conditions. As can be seen in the figure, the static aeroelastic deformation tends to unload the vehicle, thus resulting in the modified pressure distribution, particularly in the region of the wing.

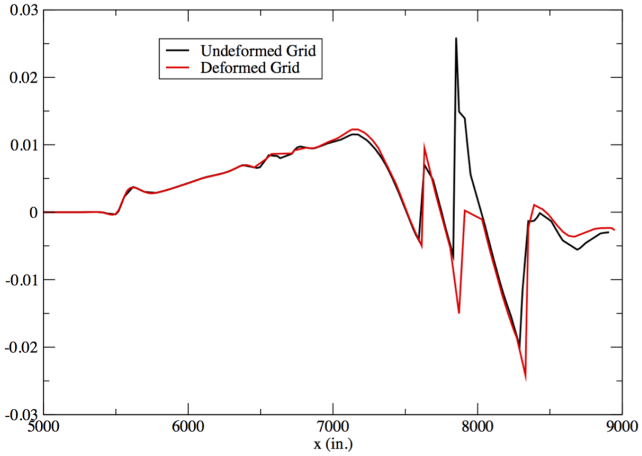

Figure 26: Near-field pressure distribution for the undeformed and deformed configurations.

6 REDUCED ORDER MODELS

The goal behind the development of a ROM for the rapid computation of unsteady aerodynamic and aeroelastic responses is aimed at addressing two challenges. The first chal-

Downloaded by NASA LANGLEY RESEARCH CENTRE on January 12, 2015 | http://arc.aiaa.org | DOI: 10.2514/6.2015-0684

lenge is the computational cost associated with full CFD aeroelastic simulations, which increases with the fidelity of the nonlinear aerodynamic equations to be solved as well as the complexity of the configuration. Computational cost, however, may be reduced via the implementation of parallel processing techniques, advanced algorithms, and improved computer hardware processing speeds.

The second, more serious, challenge is that the information generated by these simulations cannot be used effectively within a preliminary design environment. Because the output of these full CFD aeroelastic simulations cannot be incorporated within a design environment, parametric variations and design studies can only be performed by trial-and-error. As a result, the integration of computational aeroelastic simulations into preliminary design activities involving disciplines such as aeroelasticity, aeroservoelasticity (ASE), and optimization continues to be a costly and impractical venture.

However, with the development of reduced-order modeling (ROM) methods [20–22], the rapid generation of root locus plots using CFD-based unsteady aerodynamics is now available to aeroelasticians. This recently developed technology is being applied to the N+2 supersonic configuration for evaluation of aeroelastic mechanisms across several Mach numbers. A sample of some of those results is presented in the following.

An aeroelastic ROM has been developed at the cruise Mach number of 1.7. Presented in Figure 28 is a comparison of the dynamic aeroelastic response from a full FUN3Dv12 aeroelastic solution and the ROM aeroelastic solution at a dynamic pressure of 2.149 psi where the time histories of the fourth mode generalized displacements are compared. As can be seen, the results are practically identical. Similar results are obtained for all the other modes, indicating good confidence in the ROM.

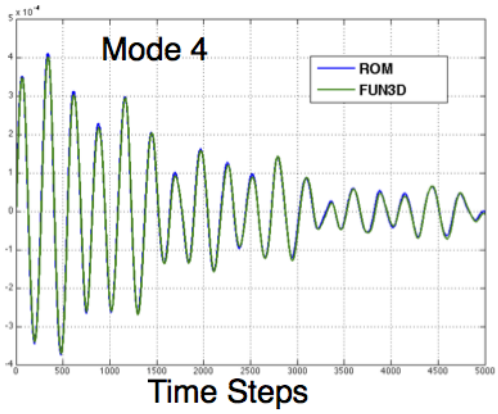

Figure 27: Comparison of full FUN3Dv12 aeroelastic response and ROM aeroelastic response for the fourth mode at M=1.7 and a dynamic pressure of 2.149 psi.

A major benefit of this ROM technology is the ability to rapidly generate an aeroelastic root locus plot that reveals the aeroelastic mechanisms occurring at that flight condition. Presented in Figure 29 is the aeroelastic root locus plot with a variation in dynamic pressure. As can be seen, the flutter mechanism is related to a coalescence of the fifth and sixth modes. There also appears to be an interesting blending of the second and fourth

Downloaded by NASA LANGLEY RESEARCH CENTRE on January 12, 2015 | http://arc.aiaa.org | DOI: 10.2514/6.2015-0684

modes.

The computational cost of generating these ROM solutions consists of one full FUN3Dv12 solution that is used to generate the ROM at that Mach number. This full FUN3Dv12 solution ran for three hours and consisted of 2400 time steps. Once this solution is available, a ROM can be generated and then used to generate all the aeroelastic responses at all dynamic pressures. In comparison, a full FUN3Dv12 analysis at each dynamic pressure requires two full FUN3Dv12 solutions: a static aeroelastic (10 hours) and a dynamic aeroelastic (18 hours). Therefore, full FUN3Dv12 solutions for 20 dynamic pressures would require 560 hours of compute time.

In the root locus plot, each symbol represents the aeroelastic roots at a specific dynamic pressure. In this case, each increment in dynamic pressure corresponds to 1 psi. It is important to mention that this root locus plot is generated in seconds while multiple full FUN3Dv12 solutions would be required for each dynamic pressure of interest.

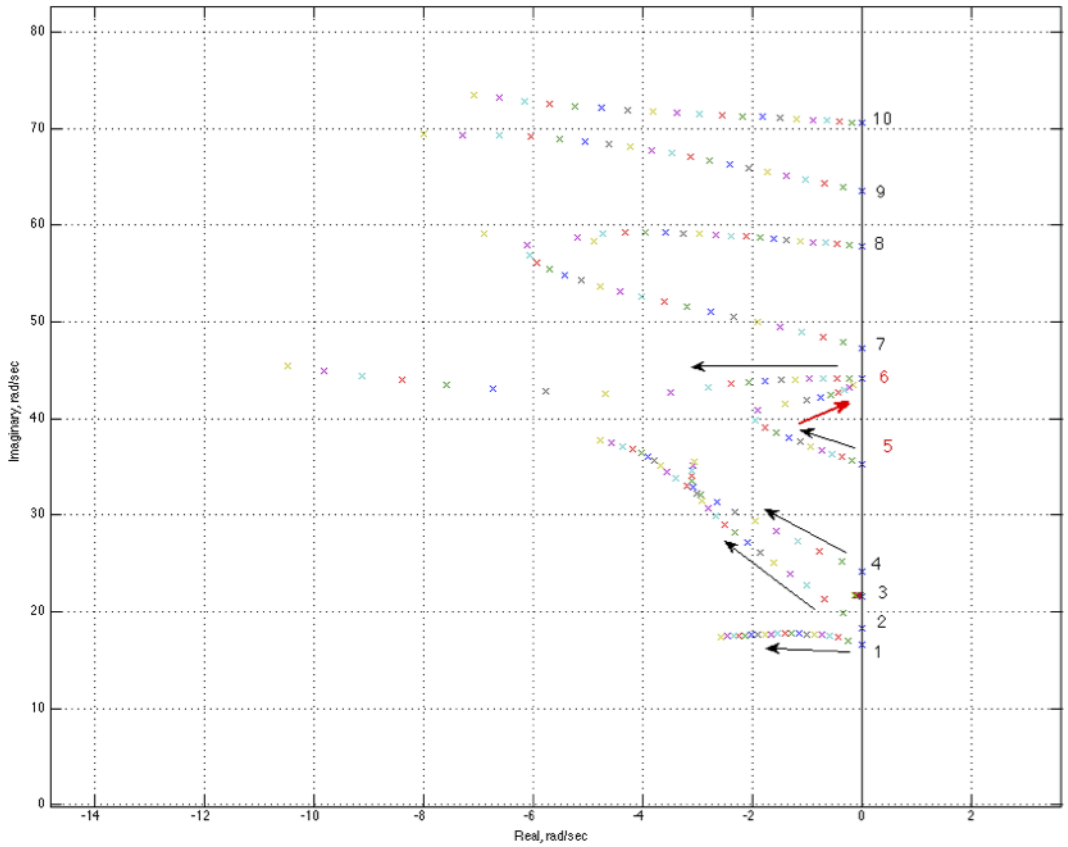

Figure 28: Aeroelastic root locus plot for the cruise condition at M=1.7 with each colored marker indicating a different dynamic pressure for a given mode.

Downloaded by NASA LANGLEY RESEARCH CENTRE on January 12, 2015 | http://arc.aiaa.org | DOI: 10.2514/6.2015-0684

7 CFL3D-ASE

The CFL3D-ASE code is a modified version of the CFL3Dv6 CFD code that allows for the inclusion of a state-space model of a control law enabling the simultaneous solution of a nonlinear unsteady aerodynamic solution and a control law in the loop. Presented in Figure 30 and Figure 31 are the open-loop and closed-loop results for a simple wing with control surface (modified AGARD 445.6 wing) as dynamic pressure is varied. Closed-loop results at the control law design dynamic pressure indicate that the control law stabilizes the flutter response at this condition. A continued increase in dynamic pressure will eventually lead to a condition that cannot be stabilized by the control law.

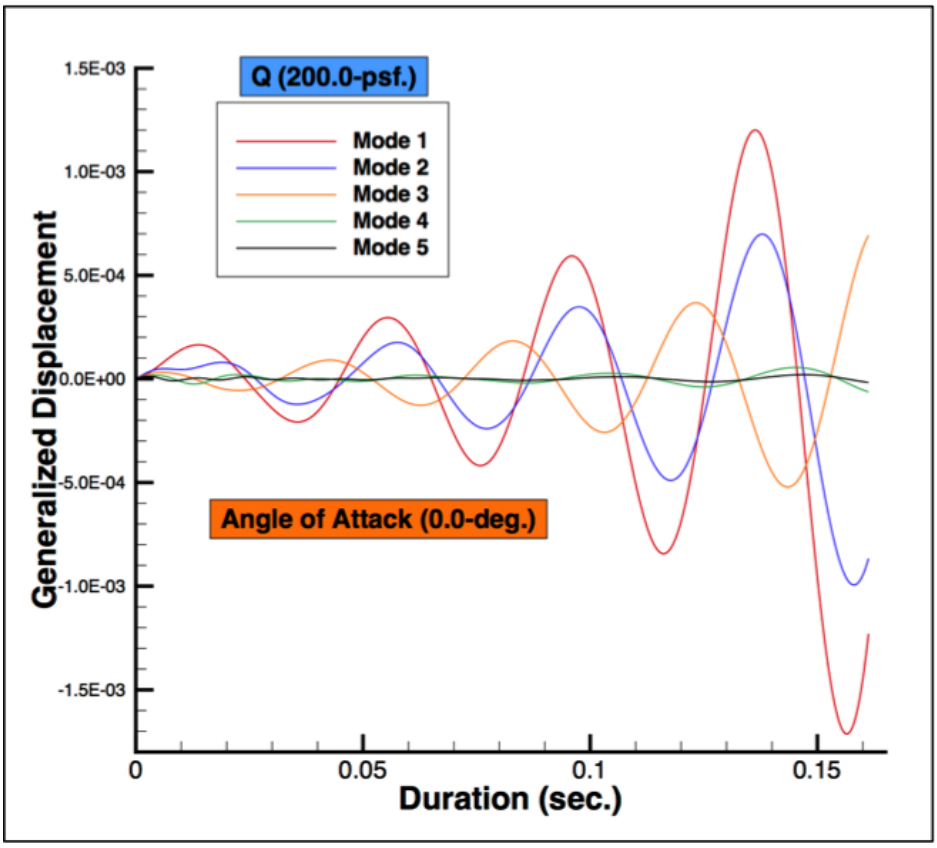

Figure 29: Application of CFL3D-ASE: open-loop result.

Results for a simple wing configuration have been completed and used to validate the method. Current work involves application of this method to a more complex supersonic aeroelastic configuration.

Downloaded by NASA LANGLEY RESEARCH CENTRE on January 12, 2015 | http://arc.aiaa.org | DOI: 10.2514/6.2015-0684

Downloaded by NASA LANGLEY RESEARCH CENTRE on January 12, 2015 | http://arc.aiaa.org | DOI: 10.2514/6.2015-0684

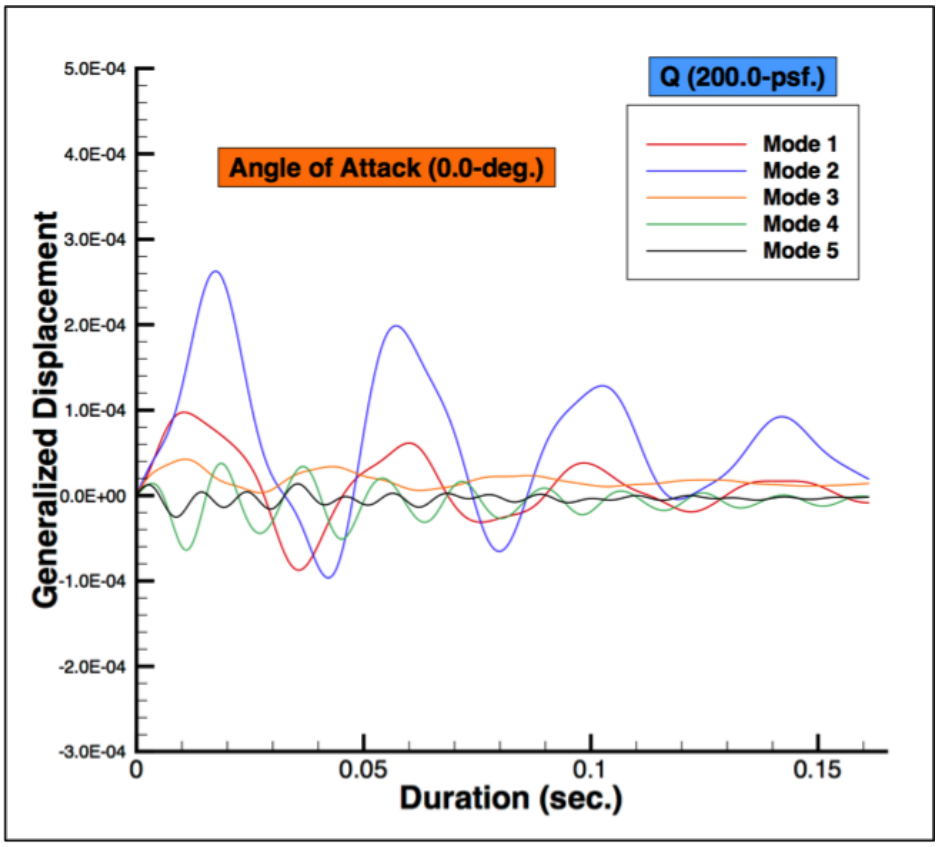

Figure 30: Application of CFL3D-ASE: closed-loop result.

8 CONCLUDING REMARKS

A summary of recent developments performed by NASA's High Speed-ASE project was presented. The summary included a discussion of the low-boom N+2 configuration and related FEM developed by Lockheed-Martin. Recent results include linear flutter boundaries based on updated and improved versions of the original FEM. Structured and unstructured CFD grids (inviscid, viscous, with/without engines) were generated and used with the CFL3Dv6 and the FUN3Dv12 CFD codes. Steady rigid and static aeroelastic results at a cruise condition were computed and presented including the effects of static aeroelastic deformation on the near-field sonic boom. Finally, brief overviews of the ongoing work related to the application of the ROM methodology and the CFL3D-ASE code were provided.

9 REFERENCES

[1] (1995). Advanced aeroservoelastic testing and data analysis. In *AGARD Conference Proceedings 566, NATO*.

[2] Noll, T. E. (1990). Aeroservoelasticity. In *31st AIAA/ASME/ASCE/AHS/ASC Structures, Structural Dynamics and Materials Conference*, 1990-29359. Long Beach, CA.

[3] Sandford, M. C., Abel, I., and Gray, D. L. (1975). Development and demonstration of a flutter-suppression system using active controls. In *NASA TR R-450*.

[4] Abel, I., Perry, B., and Newsom, J. R. (1982). Comparison of analytical and wind-tunnel results for flutter and gust response of a transport wing with active controls. In *NASA TP 2010*.

[5] Waszak, M. R. (1997). Robust multivariable flutter suppression for the benchmark active control technology (bact) wind-tunnel model. In *Eleventh Symposium on Structural Dynamics and Control*.

[6] Perry, B., Cole, S. R., and Miller, G. D. (1995). Summary of an active flexible wing program. In *Journal of Aircraft*, vol. 32. pp. 10–15.

[7] Pendleton, E. W., Bessette, D., Field, P. B., et al. (2000). Active aeroelastic wing flight research program technical program and model analytical development. In *Journal of Aircraft*, vol. 37.

[8] Silva, W. A., Keller, D. F., Florance, J. R., et al. (2000). Experimental steady and unsteady aerodynamic and flutter results for hsct semispan models. In *AIAA/ASME/ASCE/AHS/ASC 41st Structures, Structural Dynamics, and Materials Conference*, 2000-1697.

[9] Perry, B., Silva, W. A., Florance, J. R., et al. (2007). Plans and status of wind-tunnel testing employing an aeroservoelastic semispan model. In *48th AIAA/ASME/ASCE/AHS/ASC Structures, Structural Dynamics, and Materials Conference*, AIAA Paper No. 2007-1770. Honolulu, HI.

[10] Silva, W. A., Garza, A. D. L., Zink, P. S., et al. (2014). The nasa high speed ase project: Computational analyses of a low-boom supersonic configuration. In *55th AIAA/ASMe/ASCE/AHS/SC Structures, Structural Dynamics, and Materials Conference*, 2014-0675.

[11] http://www.mscsoftware.com/product/msc nastran.

[12] Jr., S. L. K. (1995). Splitflow: 3d unstructured cartesian/prismatic grid cfd code for complex geometries. AIAA Paper 95-0343.

[13] (1998). *Multi-Disciplinary Computing Environment Users Guide Version 3.0*. Huntsville, AL: CFD Research Corporation.

[14] Krist, S. L., Biedron, R. T., and Rumsey, C. L. (1997). Cfl3d user's manual version 5.0. Tech. rep., NASA Langley Research Center.

[15] Bartels, R. E. (2000). Mesh strategies for accurate computations of unsteady spoiler and aeroelastic problems. *AIAA Journal of Aircraft*, 37, 521–525.

[16] Bartels, R. E., Rumsey, C. L., and Biedron, R. T. (2006). Cfl3d version 6.4: General usage and aeroelastic analysis. In *NASA TM 2006 214301*.

[17] Roe, P. L. (1981). Approximate riemann solvers, parameter vectors, and difference schemes. *Journal of Computational Physics*, 43, 357–372.

Downloaded by NASA LANGLEY RESEARCH CENTRE on January 12, 2015 | http://arc.aiaa.org | DOI: 10.2514/6.2015-0684

[18] Anderson, W. K. and Bonhaus, D. L. (1994). An implicit upwind algorithm for computing turbulent flows on unstructured grids. *Computers and Fluids*, 23(1), 1–21.

[19] Biedron, R. T. and Thomas, J. L. (January 2009). Recent enhancements to the fun3d flow solver for moving mesh applications. In *47th AIAA Aerospace Sciences Meeting, Orlando, FL*.

[20] Silva, W. A. (July-August 2008). Simultaneous excitation of multiple-input/multiple-output cfd-based unsteady aerodynamic systems. *Journal of Aircraft*, 45(4), 1267–1274.

[21] Silva, W. A., Vatsa, V. N., and Biedron, R. T. Development of unsteady aerodynamic and aeroelastic reduced-order models using the fun3d code. IFASD Paper No. 2009-30, presented at the International Forum on Aeroelasticity and Structural Dynamics, Seattle, WA.

[22] Silva, W. A., Vatsa, V. N., and Biedron, R. T. Reduced-order models for the aeroelastic analyses of the ares vehicles. AIAA Paper No. 2010-4375, presented at the 28th AIAA Applied Aerodynamics Conference, Chicago, IL.

Downloaded by NASA LANGLEY RESEARCH CENTRE on January 12, 2015 | http://arc.aiaa.org | DOI: 10.2514/6.2015-0684